Surfaces and Interfaces 92 (2026) 109346

Contents lists available at ScienceDirect

Surfaces and Interfaces

journal homepage: www.sciencedirect.com/journal/surfaces-and-interfaces

Harnessing $Ni_xZn_{1-x}Co_2S_4$ sulfide electrode materials for enhanced supercapacitor performance and electrocatalytic activity

Zhuokun Ge [a,c,1], Zhibiao Wang [a,1], Ziqi Wang [c], Yucai Li [c], Yunjie Ke [c], Rui Guo [c], Qingzhong Gao [c], Depeng Zhao [a,c], Fufa Wu [b], Lihua Miao [a,c,*]

[a] School of Medical Information Engineering, Shenyang Medical College, Shenyang, Liaoning, 110034, PR China
[b] Liaoning Technical University, Fuxin 123000, PR China
[c] School of New Energy, Shenyang Institute of Engineering, Shenyang, Liaoning, CN 110136, PR China

ARTICLE INFO

Keywords:
Hydrothermal synthesis
Electrocatalysis
Supercapacitor
Hydrogen evolution reaction
Oxygen evolution reaction
NiZnCoS

ABSTRACT

Along with the development of the times and the continuous elevation of people's quality of life, the necessity for progressing renewable power innovations has grown more and more urgent. Electrocatalytic technology, as a potential energy solution, is anticipated for its low impact on the ecosystem, providing new ideas for addressing global issues such as environmental pollution and the reduction of greenhouse gas emissions. A two-step hydrothermal synthesis process was employed to successfully synthesize NiZnCoS electrode materials. Notably, the material $Ni_{0.5}Zn_{1.5}Co_2S_4$ demonstrated an impressive specific capacitivity of 353.8 $F{\cdot}g^{-1}$ at 1 $A{\cdot}g^{-1}$. Additionally, when this material was prepared into a membrane electrode assembly (MEA) and tested at room temperature, it had an potential of 1.744 V at 20 $mA{\cdot}cm^{-2}$. It is noteworthy that as the testing temperature increased, the potential of this material gradually decreased, demonstrating that the electrocatalytic activity of $Ni_{0.5}Zn_{1.5}Co_2S_4$ was further enhanced at higher temperatures.

1. Introduction

With the pivotal moment of the global shift shifting from fossil fuels to renewable energy sources, electrochemical energy storage and conversion technologies are emerging due to their high efficiency [1–3]. Supercapacitors have obtained widespread applications with their rapid charging capabilities, extended cycle life, and relatively high energy density [4,5]. However, their lower energy density compared to batteries somewhat limits their wider application potential [6–8]. Electrocatalytic technology is regarded to a potential solution to cater to future energy requirements [9]. The efficiency of electrocatalytic reactions largely hinges on the kinetics of the hydrogen evolution (HER) and oxygen evolution (OER)reactions [10,11]. Notably, the slower kinetics of OER compared to HER represent a bottleneck in elevating the efficiency of water splitting [12,13]. The design of bifunctional electrocatalysts capable of efficiently catalyzing both HER and OER could simplify the integration of water splitting devices and potentially reduce associated costs [14]. In commercial electrolysis processes, precious metal-based catalysts predominate. HER catalysis is primarily carried out by Pt-based materials, while OER catalysis relies heavily on of Ir and Ru oxides. Nevertheless, the rarity, elevated cost, and inadequate stability of these noble metal catalysts restrict their viability in large-scale implementation [15,16]. Consequently, the development of novel, cost-effective, and stable electrocatalysts has become a significant research priority [17].

Among numerous scientific studies, Metal sulfides have attracted considerable attention on account of their outstanding electrochemical properties, stable performance, economic cost-effectiveness. Particularly, materials like NiZnCoS have attracted substantial research interest as supercapacitor electrode materials, owing to their high-performance specific capacitance, rapid charging and discharging rates, and outstanding cycling stability [18,19]. It will delve into the electrochemical behavior of this material from both supercapacitor and electrocatalysis perspectives [20]. In the field of supercapacitor applications, materials are tested to analyze their charge-discharge characteristics, as well as their performance in terms of power density and energy density. In the context of electrocatalysis, the oxygen evolution (OER) and hydrogen evolution (HER) reactions, as key steps in the

* Corresponding author.
E-mail address: miaolihua@symc.edu.cn (L. Miao).
[1] These authors are co-first authors with equal contributions to this study.

https://doi.org/10.1016/j.surfin.2026.109346
Received 7 March 2026; Received in revised form 16 April 2026; Accepted 19 April 2026
Available online 20 April 2026

electrochemical water splitting process, will be further investigated for their catalytic activity, stability, and contribution to the overall efficiency of water splitting [21–23]. Through these comprehensive assessments, we aim to uncover the potential of NiZnCoS in electrochemical energy storage and transformation technologies, and its potential role in advancing new energy technologies [24].

This study successfully synthesized NiZnCoS material on onto nickel foam through hydrothermal synthesis processes. By modifying the concentration ratio of Ni^{2+} relative to Zn^{2+}, the electrochemical characteristics of the NiZnCoS electrode were investigated. In a 3.0 M KOH electrolyte, the $Ni_{0.5}Zn_{1.5}Co_2S_4$ composite showcased a specific capacitance of 353.8 $F{\cdot}g^{-1}$ at 1$A{\cdot}g^{-1}$. Additionally, the material had a low voltage of 1.69 V at 50 $mA{\cdot}cm^{-2}$ before cycling and maintained a current density of 78.9% after 50 h of cycling, demonstrating excellent stability. The sample was converted into a membrane electrode assembly (MEA) and underwent in-depth electrochemical performance evaluation. At room temperature, the potential of the MEA at 10 $mA{\cdot}cm^{-2}$ was 1.674 V. This data is significant for assessing the efficiency of electrocatalysts in practical applications. As the testing temperature increased, a gradual decrease in potential was observed, indicating that the sample possesses better electrocatalytic activity at higher temperatures.

2. Experiment

2.1. Preparation of NiZnCoS electrocatalyst samples

In this experimental procedure, urea and ammonium fluoride were employed as precipitating agents to synthesize NiZnCoS through the hydrothermal method. Varying amounts of $Ni(NO_3)_2{\cdot}6H_2O$ were used, specifically 0 mmol, 0.5 mmol, 1 mmol, 1.5 mmol, and 2 mmol, while the corresponding amounts of $Zn(NO_3)_2{\cdot}6H_2O$ were 2 mmol, 1.5 mmol, 1 mmol, 0.5 mmol, and 0 mmol. These reagents were mixed with 2 mmol $Co(NO_3)_2{\cdot}6H_2O$, 4 mmol urea, and 5 mmol ammonium fluoride in 60 ml of deionized water, stirred on a magnetic stirrer for 20 min, and then transferred to an autoclave for a reaction at 120 °C for 5 h. Afterward, the resulting products were washed and dried. The prepared precursors were further subjected to a second hydrothermal treatment in 60 ml of deionized water containing 0.35 g of $Na_2S{\cdot}9H_2O$, maintaining the reaction at 120 °C for an additional 4 h.

2.2. Electrocatalytic performance characterization

The supercapacitive and electrocatalytic characteristics were all measured using a CHI660E electrochemical workstation. For supercapacitor measurements, a 3 M KOH electrolyte was used, while a 1 M KOH electrolyte was employed for electrocatalysis. A standard three-electrode system was utilized, with the prepared samples serving as the working electrode. A Hg/HgO electrode was used as the reference electrode for supercapacitor measurements and the reference electrode for electrocatalysis. A platinum (Pt) foil was used as the counter electrode. The tests included cyclic voltammetry (CV), constant current charge-discharge (CP), LSV, electrochemical impedance spectroscopy (EIS), and cyclic stability tests (it). The voltages for the hydrogen evolution reaction (HER) and OER were converted to values relative to the reversible hydrogen electrode (RHE) using the following formula:$E_{RHE} = E + 0.098 + 0.059 \times pH$. Besides, the comprehensive water splitting performance evaluations were conducted employing a two-electrode configuration with a scan rate of 5 $mV{\cdot}dec^{-1}$.

3. Results and discussion

The crystal structure traits of the fabricated specimens were examined using XRD, as displayed in Fig. 1a. The three prominent diffraction peaks in the figure stem from the nickel foam matrix. The diffraction peaks located at 2θ of 56.6°, 49.4°, and 31.1° correspond to the (118) plane of ZnS (PDF#39–1363), the (220) plane of Ni_3S_2 (PDF#27–0341), and the (222) plane of Co_9S_8 (PDF#02–1459), respectively [25,26]. The diffraction peaks of $ZnS/Ni_3S_2/Co_9S_8$ mentioned above are essentially

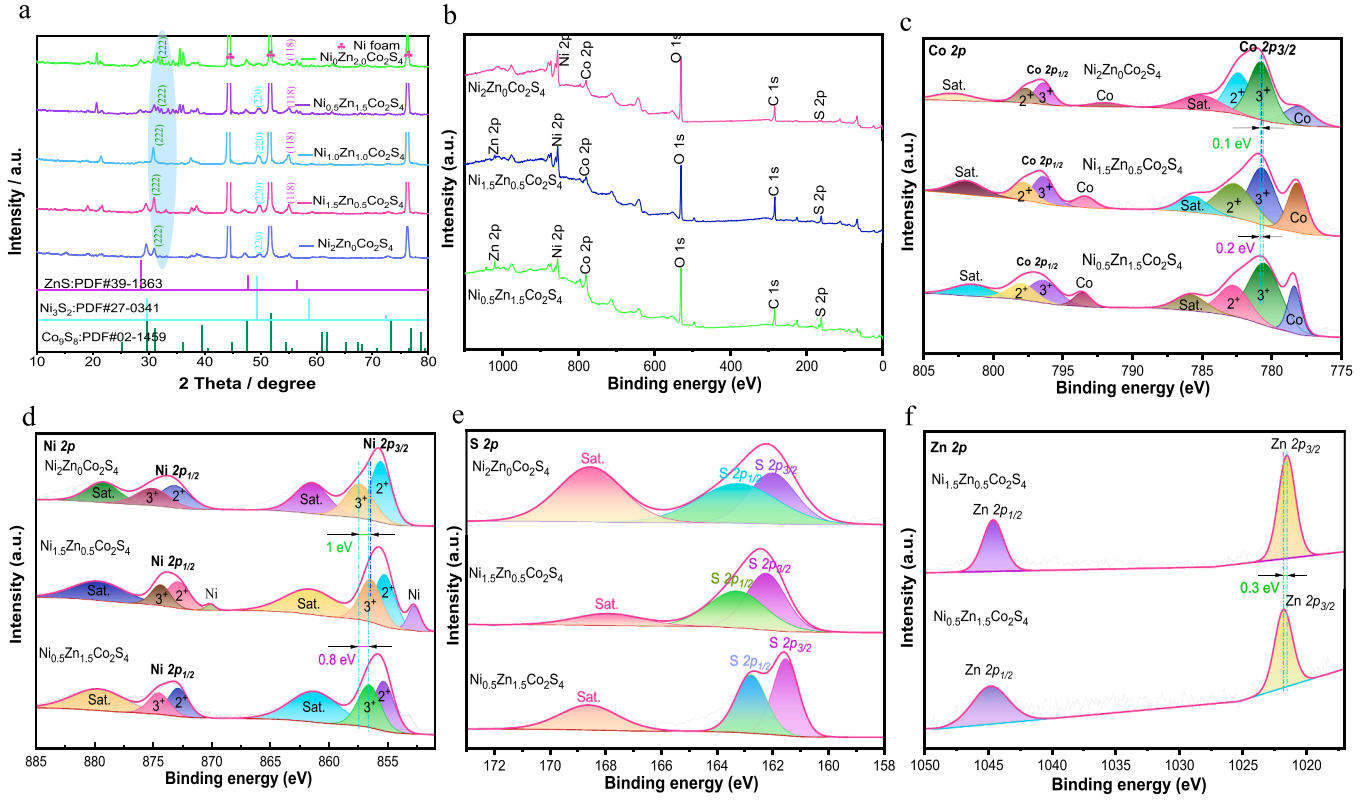

Fig. 1. (a) Structure characterization of as-fabricated samples a XRD patterns (b) The content of different elements XPS of (c) Co 2p (d) Ni 2p (e) S 2p (f) Zn 2p.

consistent with the diffraction peaks of the prepared samples, indicating that ZnS/Ni_3S_2/Co_9S_8 nanophase has been successfully grown on the foam Ni matrix through the hydrothermal synthesis method. The figure also demonstrates that with the gradual elevation of Ni^{2+}concentration, there is a concurrent reduction in Zn^{2+} concentration, the diffraction peaks slightly shift towards a higher diffraction angle, resulting in an increase in lattice spacing.

The chemical composition, elemental valence, and binding energy of the prepared samples $Ni_2Zn_0Co_2S_4$, $Ni_{1.5}Zn_{0.5}Co_2S_4$, and $Ni_{0.5}Zn_{1.5}Co_2S_4$ were deeply analyzed and compared using XPS technology. As shown in Fig. 1b, the full spectrum of all samples displayed five distinct signal peaks for Ni, Co, S, O, and C, validating the occurrence of these elements. Additionally, the elements of Zn were detected in the samples of $Ni_{1.5}Zn_{0.5}Co_2S_4$ and $Ni_{0.5}Zn_{1.5}Co_2S_4$. Meanwhile the percentage value of Co, Ni, S, and C in the $Ni_2Zn_0Co_2S_4$ sample were 6.81%, 31.1%, 6.34%, and 55.75%, respectively. In the $Ni_{1.5}Zn_{0.5}Co_2S_4$ sample, the percentages of Zn, Co, Ni, S, and C were 1.74%, 6.23%, 19.48%, 12.63%, and 59.92%, respectively. In the $Ni_{0.5}Zn_{1.5}Co_2S_4$ sample, the percentages of Zn, Co, Ni, S, and C were 3.3%, 12.54%, 13.99%, 22.11%, and 48.07%, respectively, further verifying the presence of these elements in Figure S1. Fig. 1c presents the Co 2p spectra of $Ni_2Zn_0Co_2S_4$, $Ni_{1.5}Zn_{0.5}Co_2S_4$, and $Ni_{0.5}Zn_{1.5}Co_2S_4$. The peaks at 797.78 eV and 782.38 eV correspond to Co $2p_{1/2}$ and Co $2p_{3/2}$, indicating the presence of Co^{2+} [27,28]. The peaks at 796.48 eV and 780.78 eV correspond to Co $2p_{1/2}$ and Co $2p_{3/2}$, indicating the presence of Co^{3+}. The two significant broad peaks at 802.88 eV and 785.28 eV correspond to the satellite peaks of Co $2p_{1/2}$ and Co $2p_{3/2}$, with the electron binding energy of the characteristic peaks of $Ni_{1.5}Zn_{0.5}Co_2S_4$ and $Ni_{0.5}Zn_{1.5}Co_2S_4$ differing from that of $Ni_2Zn_0Co_2S_4$ by 0.1 eV and 0.2 eV in the respective sequence [29]. Fig. 1d shows the Ni 2p spectra of the aforementioned three samples, where Ni is fit77ted to six characteristic peaks, with the peaks at 855.58 eV and 872.98 eV corresponding to Ni^{2+} $2p_{3/2}$ and Ni^{2+} $2p_{1/2}$, respectively [30,31]. The peaks at 857.38 eV and 875.08 eV belong to Ni^{3+} $2p_{3/2}$ and Ni^{3+} $2p_{1/2}$, respectively [32,33]. The two significant broad peaks at 861.38 eV and 879.28 eV correspond to the satellite peaks of Ni $2p_{3/2}$ and Ni $2p_{1/2}$, with the electron binding energy between them differing by 1 eV and 0.8 eV, respectively [34]. Fig. 1e presents the S 2p spectra of the samples $Ni_2Zn_0Co_2S_4$, $Ni_{1.5}Zn_{0.5}Co_2S_4$, and $Ni_{0.5}Zn_{1.5}Co_2S_4$, with the peaks at 163.38 eV and 161.98 eV belonging to S $2p_{1/2}$ and S $2p_{3/2}$, respectively, and the significant broad peak at 168.58 eV corresponding to the satellite peak of S 2p Fig. 1f shows the Zn 2p spectra of the samples $Ni_{1.5}Zn_{0.5}Co_2S_4$ and $Ni_{0.5}Zn_{1.5}Co_2S_4$, with the peaks at 1044.78 eV and 1021.38 eV belonging to Zn $2p_{1/2}$ and Zn $2p_{3/2}$, respectively, indicating the presence of Zn^{2+} [35–38].The multiphase sulfide structure, the coexistence of ZnS, Ni_3S_2, and Co_9S_8 phases creates abundant heterogeneous interfaces within the composite. These phase boundaries serve as unique sites for charge redistribution, where differences in work functions and electronic structures across the phases induce local charge accumulation or depletion. Such interfacial effects can lower the activation energy for key reaction steps and promote the formation of catalytically active centers. Additionally, the multiphase architecture offers complementary functionalities: Ni3S2 provides high electrical conductivity, ensuring efficient charge transport throughout the electrode. Co_9S_8 supplies a high density of redox-active sites with favorable adsorption energetics, and ZnS contributes to structural stability, preserving the integrity of the composite during prolonged operation.The electron binding energy of the characteristic peaks of $Ni_{0.5}Zn_{1.5}Co_2S_4$ differs from that of $Ni_2Zn_0Co_2S_4$ by 0.3 eV.catalytic active sites are distributed across these interfaces and modulated by synergistic electronic interactions, with the optimal Ni/Zn ratio yielding both optimized electronic structure and maximized interfacial active sites, which collectively account for the superior performance of $Ni_{0.5}Zn_{1.5}Co_2S_4$.

Figure S2a shows the microstructure of the $Ni_2Zn_0Co_2S_4$ sample at low magnification, where aggregated particulate matter with a rough surface can be observed. Figure S2b presents the microstructure of the $Ni_{1.5}Zn_{0.5}Co_2S_4$ sample at 1 um, where the sample appears as an aggregate composed of many small particles with a porous surface. Figure S2c shows the microstructure of this sample, where the fibers are interwoven, forming a complex network. The microstructure of the sample $Ni_{1.0}Zn_{1.0}Co_2S_4$, as seen in Figures S2(d-e), exhibits a porous web-like structure on the surface with varying pore sizes, distributed relatively evenly, and these fibers are interlaced to form a complex three-dimensional network. Figures S2f display the microstructure of the sample $Ni_{0.5}Zn_{1.5}Co_2S_4$, which exhibits a unique microstructure resembling coral or dendritic shapes, a structure that is significant for applications in catalysis and adsorption. At the high magnification of Figure S2g, it shows a highly complex fibrous structure. These fibers are interlaced, creating a dense network, which significantly affects the adsorption properties of the material. From Figures S2h, one can see that at the 10 um scale, the surface of the $Ni_0Zn_2Co_2S_4$ sample presents a microstructure similar to spines or needles.These morphology are conducive to the enhancement of the specific surface area. At the 100 nm scale, a more refined fibrous structure can be observed, which is related to the spine-like structures in Figure S2i, further revealing the micro-details of the material.

The prepared NiZnCoS electrode materials were subjected to electrochemical performance testing. Figures S3(a-d) display the +CV curves of $Ni_2Zn_0Co_2S_4$, $Ni_{1.5}Zn_{0.5}Co_2S_4$, $Ni_{1.0}Zn_{1.0}Co_2S_4$, and $Ni_0Zn_2Co_2S_4$ at 5 mV/s to 50 mV/s, with a test voltage range set to 0–0.6 V. It can be clearly observed from the figures that the CV curves of all samples show highly symmetrical redox peaks, indicating that the electrode materials undergo reversible Faradaic pseudocapacitive reactions. As the scan rate increases, all curves maintain their original shape, and the peak current of the CV curves increases notably with the gradual rise in scan rate, reflecting the excellent current response capability of the NiZnCoS electrode to voltage changes. Figures S3(e-h) depict the constant current charge-discharge behavior of the samples at different current densities, covering a range of 0.5, 1, 2, 4, 6, 8, and 10 $A{\cdot}g^{-1}$. At 0.5 $A{\cdot}g^{-1}$, the specific capacitance values of the samples are 147.3 $F{\cdot}g^{-1}$, 153.7 $F{\cdot}g^{-1}$, 278.5 $F{\cdot}g^{-1}$, and 360.25 $F{\cdot}g^{-1}$, respectively. Figures S3(i-l) further illustrate the constant current charge-discharge behavior of the electrode materials at a series of current densities, namely 1, 2, 4, 6, 8, 10 $mA{\cdot}cm^{-2}$, the tests were conducted. Under the current density condition of 1 $mA{\cdot}cm^{-2}$, the specific capacitance values reach 470.8 $F{\cdot}cm^{-2}$, 645.3 $F{\cdot}cm^{-2}$, 866.5 $F{\cdot}cm^{-2}$, and 1411.8 $F{\cdot}cm^{-2}$, respectively, showing the maximum specific capacitance of the capacitors at this current density. With an increase in current density, the specific capacitance values of the capacitors decline steadily, which may be due to the increased current density leading to a greater accumulation of positive and negative ions at the electrode ends, a decrease in electrolyte concentration, thereby intensifying concentration polarization, reducing the number of ions participating in the reaction, and resulting in a decrease in the capacitor's specific capacitance. Figure S4a shows the CV curves of the $Ni_{0.5}Zn_{1.5}Co_2S_4$ sample, and the symmetry of the redox peaks indicates that reversible Faradaic pseudocapacitive reactions occur in the electrode material. As the scan rate increases, the curve shape remains unchanged, showing excellent rate performance and electron transfer capability of the $Ni_{0.5}Zn_{1.5}Co_2S_4$ electrode. The shift of the redox peaks towards the ends is due to the faster change in applied voltage, with ion transport in the electrolyte not being sufficient to support the redox reactions, leading to a lag in the redox peaks. Figure S4b shows the constant current charge-discharge behavior of $Ni_{0.5}Zn_{1.5}Co_2S_4$ at different current densities, with 399.3 and 353.8 $F{\cdot}g^{-1}$ specific capacitance at 0.5 and 1 $A{\cdot}g^{-1}$ current densities, respectively. In Figure S4c, at 1 and 10 $mA{\cdot}cm^{-2}$, the magnitudes of specific capacitance are 1434.6 and 5535.7 $F{\cdot}cm^{-2}$, respectively. The basic symmetry of the curves indicates that the $Ni_{0.5}Zn_{1.5}Co_2S_4$ electrode has excellent pseudocapacitive properties.

Through TEM and high-resolution TEM (HRTEM) micrographs. The microstructure of the$Ni_{0.5}Zn_{1.5}Co_2S_4$ and $Ni_2Zn_0Co_2S_4$ samples was analyzed in detail. Fig. 2a displays the overall TEM image of the

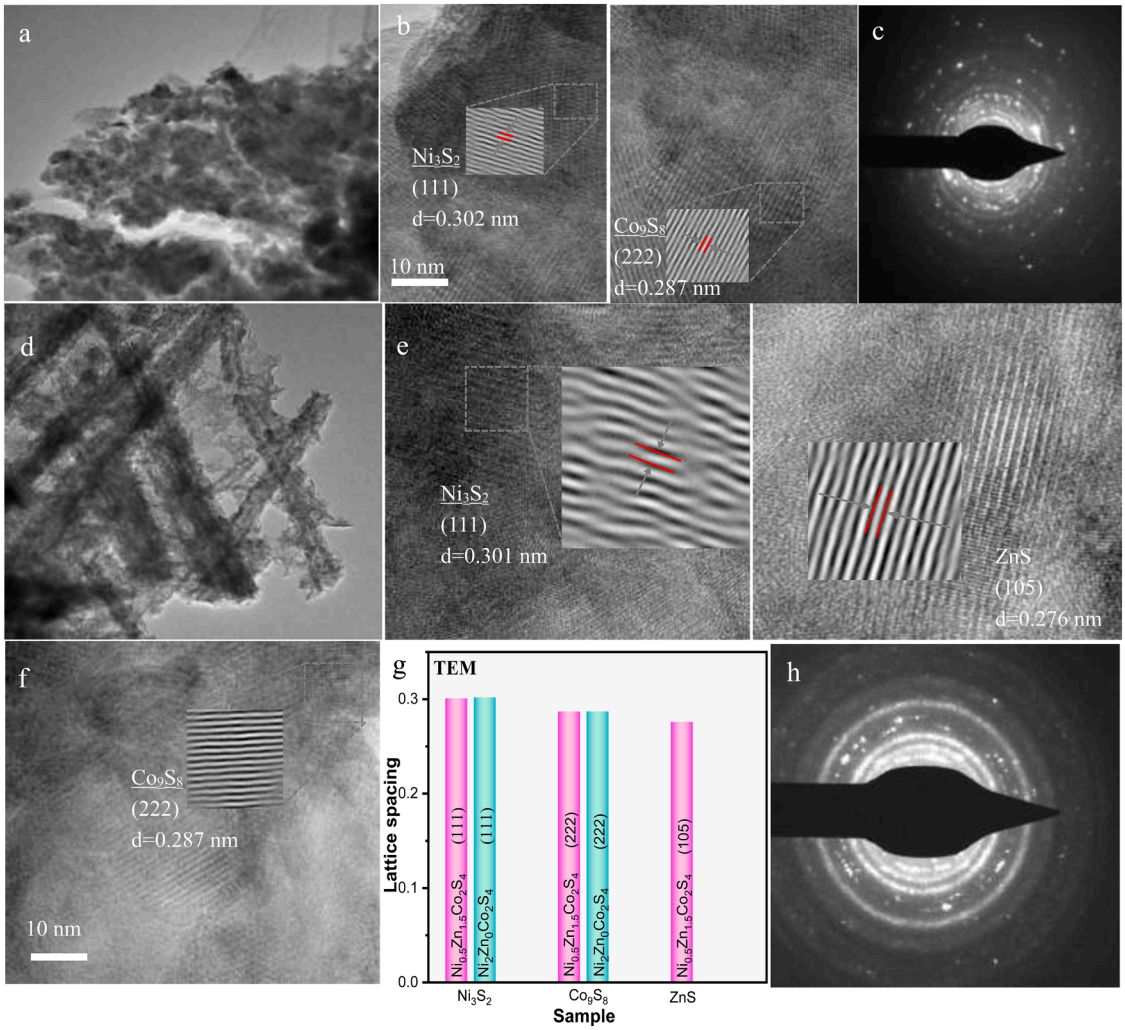

Fig. 2. $Ni_{0.5}Zn_{1.5}Co_2S_4$ morphology and structure characterization (a)TEM image of the $Ni_2Zn_0Co_2S_4$ sample (b) HRTEM image (c) SAED (d) TEM image (e-f) HRTEM image (g)lattice spacings bar chart (h) SAED.

$Ni_2Zn_0Co_2S_4$ sample, showing that the sample surface is composed of many nanoscale particles with an irregular arrangement . The HRTEM image in Fig. 2b reveals lattice spacings of 0.302 nm and 0.287 nm within the sample, which correspond to the (111) plane of Ni_3S_2 and the (222) plane of Co_9S_8, respectively. The SAED in Figure S2c indicates that the $Ni_2Zn_0Co_2S_4$ sample has a polycrystalline structure. For the $Ni_{0.5}Zn_{1.5}Co_2S_4$ sample, the TEM images in Fig. 2d indicated good control over the material synthesis process. As shown in the HRTEM images of Figures 2(e-f), lattice spacings of 0.301, 0.276, and 0.287 nm are further observed, corresponding to the (111) plane of Ni_3S_2, the (105) plane of ZnS, and the (222) plane of Co_9S_8 in that order.The bar chart in Fig. 2*g* compares the lattice spacings of the two samples, showing a slight decrease in the lattice spacings of the $Ni_{0.5}Zn_{1.5}Co_2S_4$ sample. Fig. 2h SAED,the sample shows an excellent stability.

Fig. 3a shows a comparison of the cyclic voltammetry tests of NiZnCoS electrodes with different concentrations of Ni^{2+} and Zn^{2+}at a scan rate of 10 mV/s. The figure shows oxidation peaks and reduction peaks, additionally, with higher scan rate, oxidation peaks move right and reduction peaks move left, indicating good pseudocapacitive performance, cycling performance, and charging-discharging speed. The comparison results show that the $Ni_{0.5}Zn_{1.5}Co_2S_4$ electrode exhibits superior performance. Fig. 3b shows the constant current charge-discharge relationship curves of electrodes with different concentrations of NiZnCoS at 1 $A{\cdot}g^{-1}$, with discharge times of 202.1 s, 188.6 s, 361.1 s, 530.7 s, and 393.7 s, respectively. Fig. 3c shows the discharge times at 1 $mA{\cdot}cm^{-2}$ are 706.15 s, 967.9 s, 1299.8 s, 2151.9 s, and 2117.7 s, respectively. It can be compared that the $Ni_{0.5}Zn_{1.5}Co_2S_4$ sample has the longest discharge time. Fig. 3d shows the electrochemical impedance spectroscopy (EIS) of different electrode materials at 0.01∼100 kHz. All EIS curves consist of a quasi-semicircle and a straight line. The figure shows that the equivalent resistances of the $Ni_2Zn_0Co_2S_4$, $Ni_{1.5}Zn_{0.5}Co_2S_4$, $Ni_{1.0}Zn_{1.0}Co_2S_4$, $Ni_{0.5}Zn_{1.5}Co_2S_4$, and $Ni_0Zn_2Co_2S_4$ electrodes are 0.504, 0.557, 0.487, 0.563, and 0.598 Ω, respectively. Fig. 3e shows the slope of the low-frequency straight line, with slope values of 4.29791, 4.18282, 3.59293, 2.99849, and 3.24233, respectively.To delve into the electrochemical behavior of the $Ni_{0.5}Zn_{1.5}Co_2S_4$ electrode material, employed $Ni_{0.5}Zn_{1.5}Co_2S_4$ as the cathode, activated carbon as the anode, with a 3 M KOH solution serving as the electrolyte for the assembly of an asymmetric supercapacitor. In a three-electrode test system, we conducted potential window tests on the electrode material and the activated carbon electrode at a scan rate of 50 mV s^{-1}, with results detailed in Fig. 3*g* It shows that the potential window of the activated carbon electrode is from −1 to 0 V, and its CV curve exhibits a rectangular characteristic with no prominent redox peaks, indicating that the activated carbon electrode displays typical characteristics of a double-layer electrode. By way of comparison, the $Ni_{0.5}Zn_{1.5}Co_2S_4$ electrode possesses a potential window ranging from 0 V to 0.6 V, and its CV curve shows a pair of characteristic redox peaks, indicating that this electrode stores energy through a Faradaic pseudocapacitive mechanism. To identify the optimal working voltage window, CV curves of the

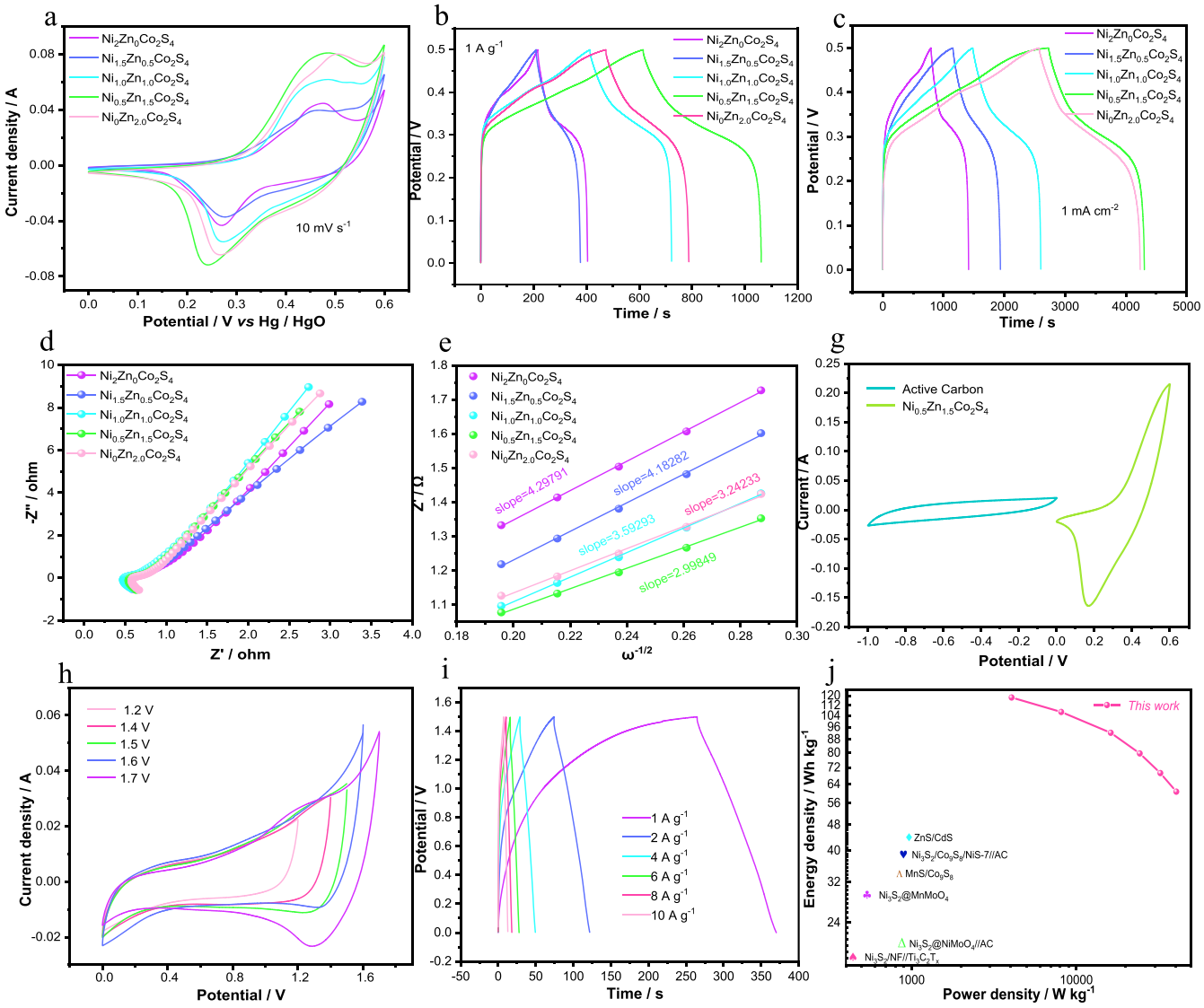

Fig. 3. (a) CV curves of different electrodes. (b) GCD curves of different electrodes. (c) GCD curves of different electrodes .(d) Impedance curves of different electrodes. (e) Graph of the slope of the oblique line in the low-frequency region of the impedance.(f) GCD curves of different electrodes (g) CV curves of different electrodes at a scanning rate of 50 mVs^{-1} (h) CV curves at different potential. (i) curves of the composite electrode.(j) Ragone of.

$Ni_{0.5}Zn_{1.5}Co_2S_4$ electrode were tested under different potential windows in a two-electrode system, with specific results shown in Fig. 3h It indicates that the composite electrode's maximum voltage can reach 1.7 V, and no obvious oxygen evolution reaction was observed, thus inferring that the most suitable potential window is 0 to 1.7 V. Figure S5a presents a series of CV curves of the $Ni_{0.5}Zn_{1.5}Co_2S_4$ electrode at different scan rates in a two-electrode system. These curves exhibit a rectangular characteristic with no distinct redox peaks, indicating that in this two-electrode system, the electrode exhibits characteristics of both double-layer capacitance and Faradaic pseudo capacitance. As the scan rate increases, the morphology of the CV curves remains consistent, demonstrating the supercapacitor's excellent capability for rapid charging and discharging. Fig. 3i depicts the curves of the composite electrode at different current densities within a potential window of 0 to 1.5 V. These curves show good symmetry, indicating the device's outstanding electrochemical performance. Figure S5b presents the electrochemical impedance spectroscopy (EIS) of the $Ni_{0.5}Zn_{1.5}Co_2S_4$ electrode material in the frequency range of 0.01 to 100 kHz. The EIS curve consists of a quasi-semicircle and a straight line. The slope of the straight line represents the electron transfer and ion diffusion resistance in the electrolyte solution at low frequencies, while the quasi-semicircle reflects the charge transfer resistance between the electrode and the electrolyte solution at high frequencies.Fig. 3j presents the Ragone plot of the assembled asymmetric supercapacitor, presenting the correlation between the energy density (E) and power density (P). It can be seen from the figure that the maximum energy density achieved by the supercapacitor is 118.5 $Wh{\cdot}kg^{-1}$, with the corresponding maximum power density of 4050 $W{\cdot}kg^{-1}$, a performance superior to other reported devices (Table 1).

After cycling the sample $Ni_{0.5}Zn_{1.5}Co_2S_4$ for 50 h, TEM analysis was conducted on it again. As shown in Figure S6a, many particles can be observed, which have undergone changes in shape and size compared to before cycling, and new pores or cracks have been generated during the cycling process, which are due to the expansion, contraction, or structural reorganization of the material. TEM analysis was conducted on it again, Figure S6b, finally, the lattice spacing of ZnS is 0.208 nm. Figure S6c SAED,the sample has good stability.Subsequently, XPS analysis was performed again on the cycled $Ni_{0.5}Zn_{1.5}Co_2S_4$ sample. Figure S7a Shows the comprehensive spectrum and elemental composition diagram of the sample before and after cycling tests, where six

Table 1
Specific capacity comparison of $Ni_{0.5}Zn_{1.5}Co_2S_4$ with other materials.

Electrocatalys	Specific Capacity (F g^{-1})	Electrolyte	Reference Electrode	reference
$Ni_{0.5}Zn_{1.5}Co_2S_4$	399.3@0.5 353.8@1	3.0 M KOH	Hg/HgO	This work
CuS@CoS_2	146@0.5 51@1	6.0 M KOH	Hg/HgO	J. Power Sources 2025.650: p. 237520.
NiCo-LDH/S-100	213@0.5 203@1	6.0 M KOH	Hg/HgO	ACS Appl. Nano Mater, 2023.6 (12): p. 10804–10816.
ONPC-900	440@0.5	6.0 M KOH	Hg/HgO	Energy Mater.2025. 5(3): p. 500024.
NCL_3	306.68@0.5	3.0 M KOH	Hg/HgO	J. Energy Storage 2024. 88: p. 111,467.
NPC	146@0.5 132@1	3.0MZn $(OTf)_2$	Hg/HgO	Carbon, 2024. 216: p. 118523.
CHPC-900	294 @0.5 300@1	6.0 M KOH	Hg/HgO	J Power Sources, 2021. 503: p. 230049.
Porous carbon	385@0.5 360@1	3.0 M KOH	Hg/HgO	J. Porous Mater. 2023. 30(5): p. 1763–1773.

elements, Co, Ni, S, Zn, O, and C, can be detected, and the content of major elements has decreased after 50 h of cycling. As shown in Figure S7b, this indicates the loss of reactants during the test reaction.

The OER performance of the prepared sample NiZnCoS was evaluated by LSV. Fig. 4a shows that at 20 mA cm^{-2}, the OER overpotential of the $Ni_{0.5}Zn_{1.5}Co_2S_4$ sample is 224.6 mV. From Figure S8a, it can be seen that the overpotential of the $Ni_{0.5}Zn_{1.5}Co_2S_4$ sample is much lower than that of $Ni_2Zn_0Co_2S_4$ (285.3mV@20mA·cm^{-2}),$Ni_{1.5}Zn_{0.5}Co_2S_4$ (260.2mV@20 mA·cm^{-2}), $Ni_{1.0}Zn_{1.0}Co_2S_4$ (247.2mV@ 20 mA·cm^{-2}), and $Ni_0Zn_2Co_2S_4$ (280.4mV@ 20 mA·cm^{-2}) samples. To gain the OER reaction kinetics of the samples, the Tafel curve was drawn based on the test date . The Tafel slope of the $Ni_{0.5}Zn_{1.5}Co_2S_4$ sample is 93.7 mV dec^{-1}in Fig. 4b, which is lower than that of $Ni_2Zn_0Co_2S_4$ (128.4 mV·dec^{-1}), $Ni_{1.5}Zn_{0.5}Co_2S_4$ (113.6 mV·dec^{-1}), $Ni_{1.0}Zn_{1.0}Co_2S_4$ (115.1 mV·dec^{-1}), and $Ni_0Zn_2Co_2S_4$ (115.9 mV·dec^{-1}), indicating that $Ni_{0.5}Zn_{1.5}Co_2S_4$ has more active sites in the OER reaction. To further refine the kinetic analysis and eliminate potential non-steady-state effects inherent to continuous scanning techniques, steady-state polarization measurements were subsequently conducted using a multi-step chronoamperometric method, as shown in Figure S7c [39]. Notably, the Tafel slopes obtained from the two methods are in excellent agreement, with the steady-state approach yielding superior linearity and reproducibility, thereby confirming the reliability and accuracy of the kinetic analysis. The electrochemical active surface area (ECSA) is a key parameter for assessing the activity of catalysts. ECSA can be explored through CV curves at different scan rates to Figure S9. Additionally, ECSA shows a proportional connection with the double-layer capacitance (Cdl), and the C_{dl} value can serve as a measure of electrocatalytic activity.The ECSA, derived from double-layer capacitance (Cdl) measurements, provides a functionally relevant metric for evaluating catalytically active sites. This relationship can be understood as follows: a higher Cdl reflects a greater abundance of accessible active sites at the electrode–electrolyte interface, thereby facilitating enhanced charge storage and electrocatalytic reactions. The larger ECSA not only provides more active sites but also promotes more efficient mass transport and charge transfer kinetics. Fig. 4c presents the C_{dl} values of the synthesized samples, with a calculated C_{dl} value of 0.03908 mF cm^{-2} for $Ni_{0.5}Zn_{1.5}Co_2S_4$. The relatively high Cdl value of $Ni_{0.5}Zn_{1.5}Co_2S_4$ indicates a larger electrochemically active surface area (ECSA), which provides more accessible active sites at the electrode–electrolyte interface and directly enhances reaction kinetics. Beyond this quantitative factor, the intrinsic activity of each site is further promoted by synergistic electronic interactions among Ni, Zn, and Co species across the multiphase boundaries (ZnS, Ni_3S_2, Co_9S_8), which facilitate charge redistribution and optimize intermediate adsorption energetics. Thus, both the enlarged ECSA and the electronic modulation at heterogeneous interfaces contribute to the superior catalytic performance. The EIS spectrum in Figure S8c shows that the slope in the low-frequency region indicates that the $Ni_{0.5}Zn_{1.5}Co_2S_4$ sample has a higher mass transport efficiency.In a 1.0 M KOH solution, the electrocatalytic hydrogen evolution reaction (HER) performance of the $Ni_{0.5}Zn_{1.5}Co_2S_4$ sample was investigated. The LSV curve corresponding to the $Ni_{0.5}Zn_{1.5}Co_2S_4$ was compared with that of the noble metal platinum/carbon (Pt/C) catalyst . From Fig. 4d and parts S8b, it can be seen that −10 mA cm^{-2}, the HER overpotential of $Ni_{0.5}Zn_{1.5}Co_2S_4$ is −134.4 mV, lower than the overpotentials of $Ni_2Zn_0Co_2S_4$ (−234.4 mV), $Ni_{1.5}Zn_{0.5}Co_2S_4$ (−180.4 mV), $Ni_{1.0}Zn_{1.0}Co_2S_4$ (−198.4 mV), and $Ni_0Zn_2Co_2S_4$ (−168.4 mV), with the exception of the Pt/C catalyst which has an HER overpotential of −43.4 mV. To gain deeper insights into the sample's HER kinetics, the Tafel slope was obtained from the LSV curves, shown in Fig. 4e.The Tafel slope of $Ni_{0.5}Zn_{1.5}Co_2S_4$ is 107.5 mV·dec^{-1}, slightly higher than that of $Ni_2Zn_0Co_2S_4$ (99.9 mV·dec^{-1}), $Ni_{1.5}Zn_{0.5}Co_2S_4$ (148.5 mV·dec^{-1}), $Ni_{1.0}Zn_{1.0}Co_2S_4$ (159.1 mV·dec^{-1}), and $Ni_0Zn_2Co_2S_4$ (121.1 mV·dec^{-1}), indicating that $Ni_{0.5}Zn_{1.5}Co_2S_4$ has a higher intrinsic activity. To investigate the reason for the enhanced HER activity, the electrochemical active surface area (ECSA). As the ECSA shows a proportional relationship with the double-layer capacitance (Cdl) at the electrode/solution interface, ECSA can be determined by quantitative analysis of C_{dl}, as shown in Figure S10a. Calculated from parts S10(b-f), the C_{dl} of the $Ni_{0.5}Zn_{1.5}Co_2S_4$ catalyst is 0.01633 mF·cm^{-2}, while the C_{dl} values for the other samples are $Ni_2Zn_0Co_2S_4$ (0.00947 mF·cm^{-2}), $Ni_{1.5}Zn_{0.5}Co_2S_4$ (0.028 mF·cm^{-2}), $Ni_{1.0}Zn_{1.0}Co_2S_4$ (0.02675 mF·cm^{-2}), and $Ni_0Zn_2Co_2S_4$ (0.14127 mF·cm^{-2}). The $Ni_{0.5}Zn_{1.5}Co_2S_4$ catalyst exhibits an outstanding ECSA. The radar chart in Fig. 4f shows that among the NiZnCoS series, the $Ni_{0.5}Zn_{1.5}Co_2S_4$ sample demonstrates exceptional electrocatalytic performance in both the oxygen evolution reaction (OER) and hydrogen evolution reaction (HER) in alkaline environments. As shown in Figure S11, post-stability XRD analysis confirms that the bulk multiphase structure of $Ni_{0.5}Zn_{1.5}Co_2S_4$ is well preserved after 50 h of OER testing, with diffraction peaks corresponding to ZnS, Ni_3S_2, and Co_9S_8 remaining clearly identifiable. Minor surface reconstruction is also observed, contributing to the formation of a stable architecture that underpins the material's high catalytic activity and exceptional durability.XPS analysis was performed again on the cycled $Ni_{0.5}Zn_{1.5}Co_2S_4$ sample, Co 2p (Fig. 4*g*) peak position also remains essentially unchanged. This indicates that the $Ni_{0.5}Zn_{1.5}Co_2S_4$ sample has good stability. In Figs. 4h no significant changes were found in Zn 2p, further demonstrating this stable state after cycling. Fig. 4i displays the Ni 2p spectrum of the $Ni_{0.5}Zn_{1.5}Co_2S_4$ sample before and after cycling, with a peak shift of Ni by 0.8 eV, which shows no significant change.This indicates that the $Ni_{0.5}Zn_{1.5}Co_2S_4$ sample has good stability. In Figs. 4j, no significant changes were found in S2p, which proves the material's resilience and consistency in electrochemical applications. TEM analysis was conducted on it again. In Fig. 4k-l, it is known that the lattice spacing of Ni_3S_2 is 0.184 nm, that of Co_9S_5 is 0.222 nm.

Figure S12 presents the cyclic stability of $Ni_{0.5}Zn_{1.5}Co_2S_4$ and $Ni_2Zn_0Co_2S_4$ measured through multi-step chronoamperometry under OER conditions, showing that the $Ni_{0.5}Zn_{1.5}Co_2S_4$ sample exhibits higher stability after continuous operation for 50 h. The inset figure compares the LSV curves of $Ni_{0.5}Zn_{1.5}Co_2S_4$ and $Ni_2Zn_0Co_2S_4$. Figure S13 displays the cyclic test plots of the two samples after 10 h of operation under HER conditions, with the inset figure showing the LSV comparison under HER.

To delve into the application prospects of the electrocatalyst in the field of water splitting, we prepared samples and used them as anodes and cathodes to construct the corresponding electrochemical devices.

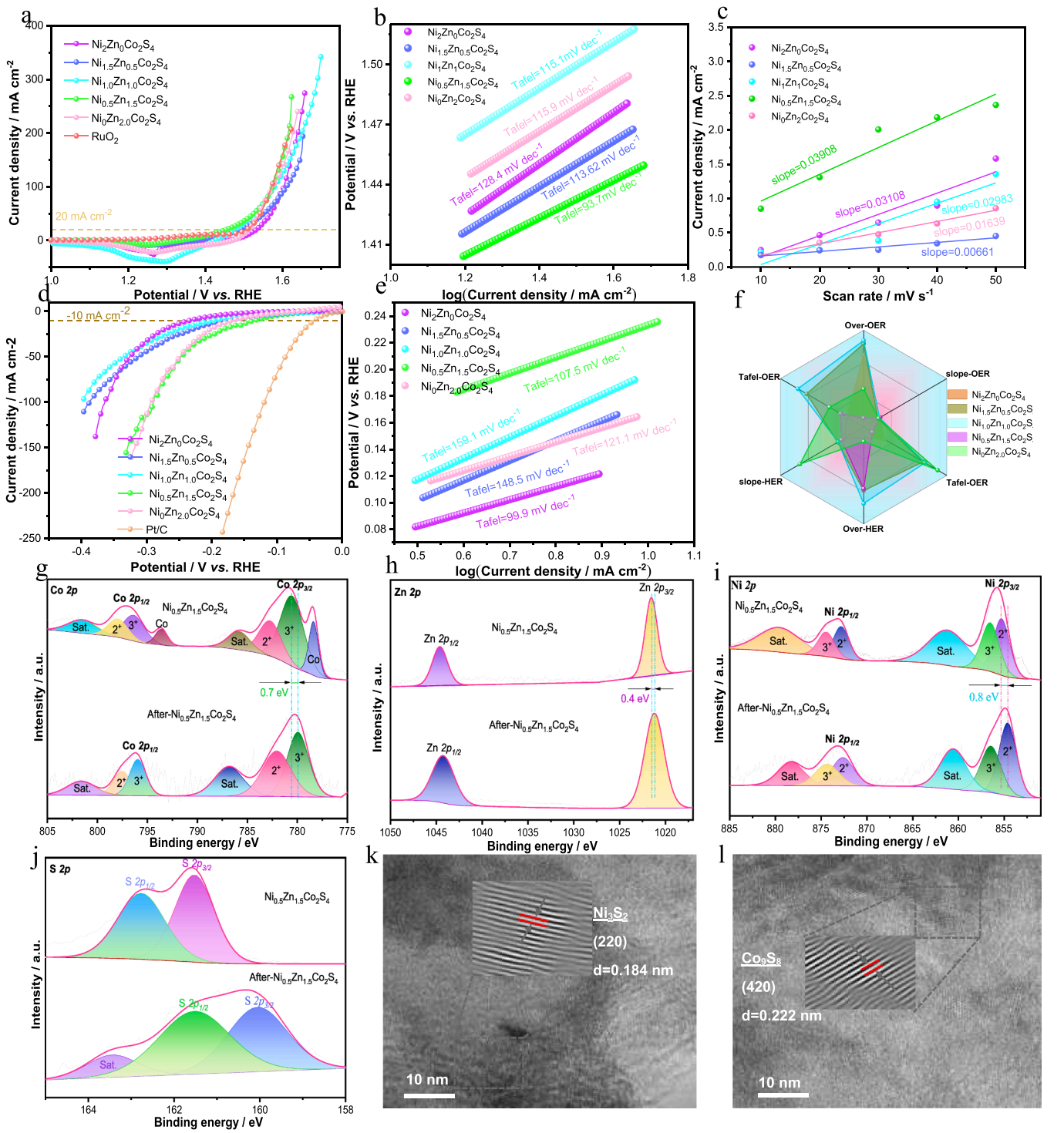

Fig. 4. (a) Curves a current density (b) Tafel slope OER (c) double-layer capacitance (Cdl) (d) curves a current density of 10 mA cm^{-2} (e) Tafel slope HER (f)Radar chart (g) Co 2p spectral (h)Zn 2p spectral.(i) Ni 2p spectral.(j) S 2p spectral.(k,l)HRTEM image.

Fig. 5a displays the linear sweep voltammetry (LSV) curves of $Ni_2Zn_0Co_2S_4$, $Ni_{0.5}Zn_{1.5}Co_2S_4$, and After-$Ni_{0.5}Zn_{1.5}Co_2S_4$ in an alkaline medium. $Ni_{0.5}Zn_{1.5}Co_2S_4$ reaches a cell voltage of 1.69 V at a current density of 50 mA·cm^{-2}, with a slight increase to 1.758 V after cycling, while the voltage for $Ni_2Zn_0Co_2S_4$ is 1.71 V. The potential of $Ni_{0.5}Zn_{1.5}Co_2S_4$ is significantly lower than that of $Ni_2Zn_0Co_2S_4$, further confirming its superior performance.Moreover, $Ni_{0.5}Zn_{1.5}Co_2S_4$ demonstrates excellent stability in an alkaline medium, as shown in Fig. 5b, with performance retention at 79.6% after 50 h of cyclic testing, highlighting the potential of this sample for sustained catalytic activity in water splitting reactions.Fig. 5c is the Bode plot for the $Ni_{0.5}Zn_{1.5}Co_2S_4$ sample, where the phase angle decreases as the voltage is increased from 1.4896 V to 1.5506 V. This indicates an acceleration in the rate of electron transfer, which is favorable for electrocatalytic reactions.To assess the feasibility of $Ni_{0.5}Zn_{1.5}Co_2S_4$ material in industrial applications, we integrated the material into a membrane electrode assembly. Both the cathode and anode are made of $Ni_{0.5}Zn_{1.5}Co_2S_4$ material, separated by an anion exchange membrane. Subsequently, we

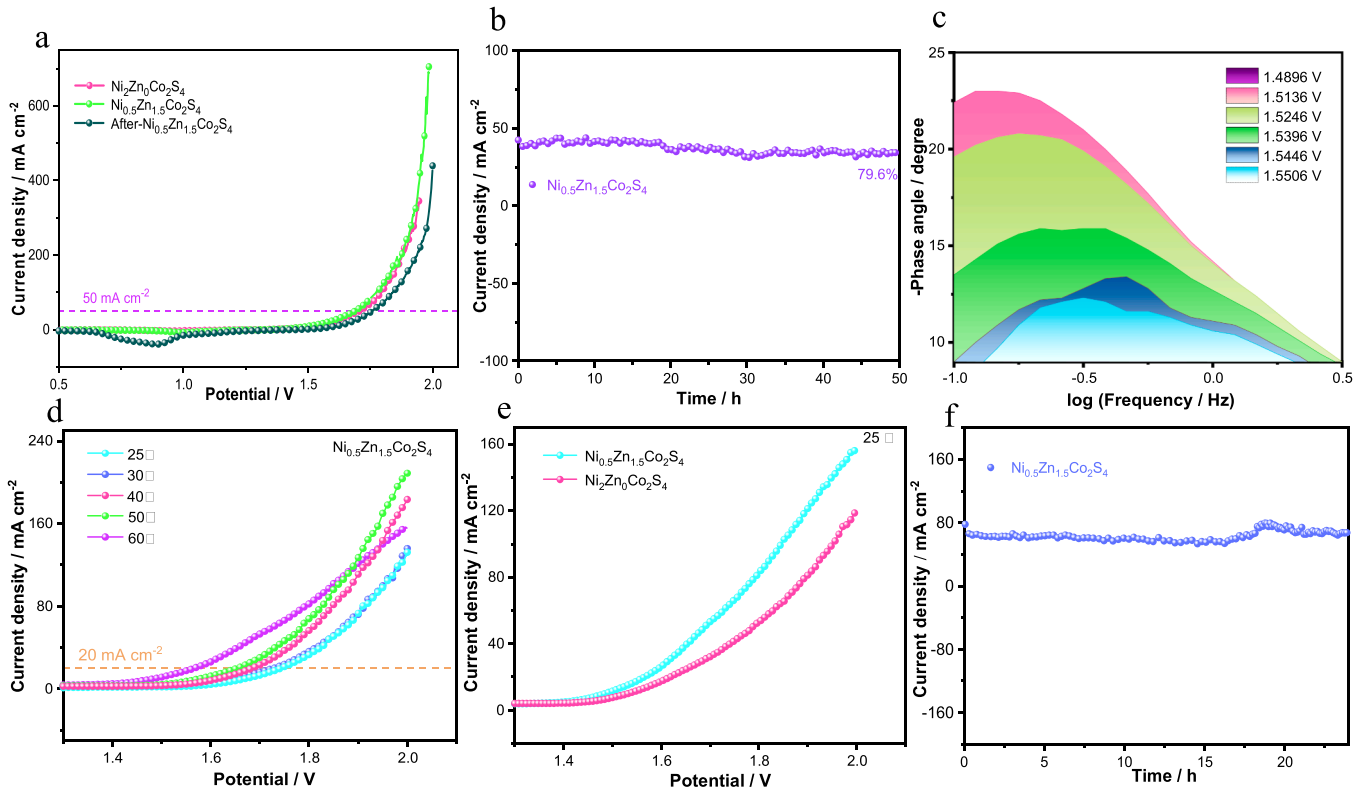

Fig. 5. (a) Linear sweep voltammetry curves (b) cyclic testing images (c) Bode plot (d) CV at differenttemperatures (e) Comparison of polarization curves for different catalysts (f) cyclic testing images.

tested the electrochemical performance of the material. Fig. 5d presents the LSV curves of $Ni_{0.5}Zn_{1.5}Co_2S_4$ at different temperatures of 25 °C, 30 °C, 40 °C, 50 °C, and 60 °C, with the corresponding potentials at a 20 mA cm^{-2} being 1.744 V, 1.73 V, 1.686 V, 1.654 V, and 1.567 V. It is noticeable that with a rise in temperature, the exchange interaction between the electrolyte and the electrode material is enhanced, leading to a gradual decrease in potential. Under ambient conditions, the LSV curve comparison between $Ni_{0.5}Zn_{1.5}Co_2S_4$ and $Ni_2Zn_0Co_2S_4$ shows that $Ni_{0.5}Zn_{1.5}Co_2S_4$ has a lower potential, as depicted in Fig. 5e. To test the stability of the sample at room temperature, we observed in Fig. 5f that even after a 24-hour cyclic test, the sample still maintains high stability.

4. Conclusion

This research successfully synthesized the $Ni_{0.5}Zn_{1.5}Co_2S_4$ electrocatalyst using hydrothermal synthesis technology. In an alkaline medium, this material demonstrates exceptional charge-discharge performance, as well as superior capabilities in both oxygen evolution reaction and hydrogen evolution reaction. Notably, in a 3.0 M KOH solution, $Ni_{0.5}Zn_{1.5}Co_2S_4$ achieves a mass-specific capacitance of 399.3 $F{\cdot}g^{-1}$ at 0.5 $A{\cdot}g^{-1}$. The asymmetric supercapacitor fabricated from $Ni_{0.5}Zn_{1.5}Co_2S_4$ delivers an energy density of 118.5 $Wh{\cdot}kg^{-1}$ with an impressive power density of 4050 $W{\cdot}kg^{-1}$. In a potassium hydroxide solution with a concentration of 1.0 M, $Ni_{0.5}Zn_{1.5}Co_2S_4$ excels in OER with the corresponding overpotential reaches 224.6 millivolts at 20 mA cm^{-2} and a Tafel slope of 93.7 mV dec^{-1}. In HER, the catalyst shows an potential of −134.4 mV at −10 $mA{\cdot}cm^{-2}$ and a Tafel slope of 107.5 $mV{\cdot}dec^{-1}$. Moreover, at 50 $mA{\cdot}cm^{-2}$, $Ni_{0.5}Zn_{1.5}Co_2S_4$ operates at the output voltage of this battery reaches 1.69 V. and retains excellent stability even after 50 h of cyclic testing. Furthermore, we fabricated a membrane electrode assembly (MEA) using $Ni_{0.5}Zn_{1.5}Co_2S_4$ and conducted a comprehensive assessment of its Electrochemical performance. At standard room temperature, the MEA exhibits an potential of 1.744 V, and it maintains remarkable stability after a 24-hour cyclic test. performance of the electrocatalyst. As the test temperature rises, the potential values decrease gradually, indicating that the material's electrocatalytic activity is enhanced at higher temperatures. This finding suggests that by adjusting the operating temperature, the electrochemical performance of the MEA can be optimized, thereby increasing the efficiency of electrocatalytic reactions. The positive impact of temperature on potential not only highlights the material's stability and activity across a range of temperatures but also opens new avenues for the prospective applications of electrochemical energy transmutation techniques. This research provides innovative insights for the design and manufacture of high-performance supercapacitors and electrocatalysts.

1. Dataset Rationality and Composition

All data were collected and processed in strict accordance with material chemistry experimental norms, ensuring their scientificity and reliability. The dataset composition is as follows:

Raw electrochemical test data: Collected via CHI660E electrochemical workstation, including cyclic voltammetry (CV), constant current charge-discharge (CP), linear sweep voltammetry (LSV), electrochemical impedance spectroscopy (EIS), and chronoamperometry (i-t) curves for cyclic stability tests. Separate records are kept for supercapacitor and electrocatalysis tests, corresponding to 3 M KOH and 1 M KOH electrolyte systems respectively.

Processed and derived data: Key parameters calculated from raw data, including supercapacitive performance indexes and electrocatalytic activity parameters (HER/OER voltages). Voltage conversion records for RHE calibration are included, with detailed calculations based on the formula: $ERHE = E + 0.098 + 0.059 \times pH$. Data from comprehensive water splitting performance evaluations (two-electrode configuration, scan rate: 5 $mV{\cdot}dec^{-1}$) are also included.

Experimental metadata: Detailed records of the three-electrode system configuration (working electrode: prepared samples; reference electrode: Hg/HgO for supercapacitors, AgCl for electrocatalysis; counter electrode: Pt foil) and two-electrode configuration for water splitting tests.

2. Experimental Data Reliability Assurance

All experimental data were obtained through standardized and repeatable procedures. The tests were conducted using a unified CHI660E electrochemical workstation, and the electrode systems and electrolytes were strictly controlled as specified, ensuring the consistency and reliability of the data. Each key performance index was verified by three parallel experiments, and the data deviation was within the acceptable range of material chemistry research.

3. Contact for Experimental Inquiries

Inquiries concernexperimental methodologies, data processing principles, or test-specificdirect correspondence to atPrompt responsesfurnishthreeFor questions regarding experimental methods, data processing principles, or test details, please contact [Corresponding Author: Depeng Zhao] (School of New Energy, Shenyang Institute of Engineering) via email: Hellodepeng@163.com.

CRediT authorship contribution statement

Zhuokun Ge: Writing – review & editing, Writing – original draft. **Zhibiao Wang:** Writing – review & editing. **Ziqi Wang:** Writing – review & editing, Writing – original draft. **Yucai Li:** Writing – review & editing. **Yunjie Ke:** Writing – review & editing. **Rui Guo:** Writing – review & editing. **Qingzhong Gao:** Writing – review & editing. **Depeng Zhao:** Writing – review & editing. **Fufa Wu:** Writing – review & editing. **Lihua Miao:** Writing – review & editing.

Declaration of competing interest

The authors declare no conflict of interest.

Supplementary materials

Supplementary material associated with this article can be found, in the online version, at doi:10.1016/j.surfin.2026.109346.

Data availability

The data that has been used is confidential.

References

[1] W. Zhang, S. Wang, C. Yang, J. Yu, Y. Guo, S. Zhang, Y. Song, X. Zhang, G. Wang, X. Bao, Dual-donor doped perovskite as bifunctional oxygen electrode catalyst for reversible protonic ceramic electrochemical cell, J. Am. Chem. Soc. (2025) 43584–43593.

[2] C. Liu, H. Bai, J. Feng, K. An, L. Li, Z. Yu, L. Qiao, D. Liu, S. Peng, H. Liu, H. Pan, Electrodeposited ternary metal (Oxy)hydroxide achieves highly efficient alkaline water electrolysis over 1000 h under industrial conditions, Carbon Energy 7 (2025) e684.

[3] E. Wang, C. Xu, M. Chen, W. Hua, X. Liu, Y. Liu, Z. Wu, Y. Xiao, W. Yang, X. Guo, W. Chen, Superstructure engineering enables NASICON-type phosphate cathodes with increased working voltage and energy density, Adv. Mater. 37 (2025) e12435.

[4] H. Hou, G. Lei, H. Huo, Y. Yu, Z. Tang, C. Qin, D. Min, CuCo-layered double hydroxide nanosheets grown on hierarchical carbonized wood as bifunctional electrode for supercapacitor and hydrogen evolution reaction, Adv. Sci. (2025) e08630.

[5] R.-Y. Li, X.-Y. Shen, J. Li, D.-P. Zhao, R.-D. Zhao, F.-F. Wu, Enhanced electrochemical performance of NiCo-layered double hydroxides: optimal synthesis conditions and supercapacitor applications, Adv. Sustain. Syst. (2024) 2400753.

[6] J. Li, Y. Dong, X. Wang, Y. Li, Q. Fan, J. Xu, H. Xie, Q. Kuang, Y. Zhao, Reconciling capacity degradation for sodium-ion pouch cell by practical electrocatalytic-driven compensation strategy, ACS Nano 19 (2025) 38016–38027.

[7] Y. Liu, L. Feng, M. Li, X. Qian, C. Sun, W. Sun, Y. Zheng, B. Li, Robust interfaces and advanced materials: critical designs and challenges for high-performance supercapacitors, Energy Environ. Mater. (2025) e70116.

[8] K. Zhao, X. Zhang, H. Xiang, Z. Zou, S. Kong, K. Cheng, Construction of core-shell structured CuS@CoS_2 via ion exchange method for flexible all-solid-state asymmetric supercapacitors, J. Power. Sources 650 (2025) 237520.

[9] L. Huang, Z. Fu, H. Yin, C. Xia, S. Cao, X. Weng, L. Shi, Z. Wu, Electrocatalytic utilization of air pollutants and GHGs: fundamentals, electrode materials, and reactors, Environ. Sci. Technol. 59 (2025) 24177–24196.

[10] Q. Wu, D. Shao, C. Dai, J. Wang, X. Li, P. Song, W. Xie, S. Xi, L. Zhang, X. Lin, S. Luo, S. Sun, L. An, P. Xi, Z.J. Xu, Efficient electrocatalytic nitrate-to-ammonia enabled by reversible lattice-oxygen control, J. Am. Chem. Soc. 147 (2025) 30401–30411.

[11] Y. Yu, Y. Yin, Y. Liu, X. Li, J. Wang, G. Qin, S. Li, Inverse ZnO/AuCu electrocatalyst enabling tunable CO-rich syngas for electrified carbon cycling in steelmaking, ACS. Appl. Mater. Interfaces 17 (2025) 62091–62099.

[12] S. Min, G. Yang, Y. Jiao, J. Wang, Y. Liu, Z. Chen, H. Yan, H. Fu, Modulation of active sites induced by CoP via Mn doping enables multifunctional electrocatalytic hydrogen evolution, oxygen evolution, and biomass oxidation reactions, Adv. Funct. Mater. (2025) e14250.

[13] H. Zhou, S. Xu, B. Zhang, X. Li, Z. Lv, D. Zhao, R.-D. Zhao, In situ reconstructed amorphous MOOH-enhanced NiCoP@NiFe-LDH bifunctional electrocatalyst for long durable seawater electrolysis, Inorg. Chem. Front. 13 (2026) 666–679.

[14] N. Zhao, N. Zhang, K. Liu, S. Liu, Y. Wang, R. Jia, Y. Dai, M. Xue, G. Zhao, Hierarchical structure based on Fe, Mo co-doped Ni_3S_2 and NiFe LDH: dual-anode boosting efficient hydrogen evolution, Nano Res. Energy 4 (2025) e9120206.

[15] Q. Li, Z. Deng, D. Tao, J. Pan, W. Xu, Z. Zhang, H. Zhong, Y. Gao, Q. Shang, Y. Ni, X. Li, Y. Chen, Q. Zhang, Edge-effect modulated noble metal electrocatalysts for efficient and pH-universal hydrogen evolution reaction, Adv. Funct. Mater. 34 (2024) 2411283.

[16] K. Zhang, K. Wang, S. Chai, L. Wang, H. Luo, Y. Liu, Y. Wang, J. Jiang, B. Li, Engineering Ru-based electrocatalysts for efficient electrocatalytic water splitting, Nano Res. 18 (2025) 94907369.

[17] R.Y. Li, S.L. Xu, Z.Q. Ai, J.G. Qi, F.F. Wu, R.D. Zhao, D.P. Zhao, Interface engineering accelerated surface reconstruction for electrocatalytic water splitting and energy storage device through hybrid structured $ZnCo_2O_4$@NiCo-LDH nanocomposite, Int. J. Hydrog. Energy 91 (2024) 867–876.

[18] M. Deng, X. Xu, W. Qiu, Y. Duan, R. Li, L. Yu, Q. Peng, Improving miscibility of polymer donor and polymer acceptor by reducing chain entanglement for realizing 18.64 % efficiency all polymer solar cells, Angew. Chem. Int. Ed. 63 (2024) e202405243.

[19] F. Li, H. Wu, S. Lv, Y. Ma, B. Wang, Y. Ren, C. Wang, Y. Shi, H. Ji, J. Gu, S. Tang, X. Meng, Two birds with one stone: contemporaneously enhancing OER catalytic activity and stability for dual-phase medium-entropy metal sulfides, Small 20 (2023) 2309025.

[20] H. Zhou, X. Li, B. Zhang, H. Ren, D. Zhao, R. Zhao, L. Miao, Interface-engineered $NiSe_2$/Ni–Fe_2P nanocubes for efficient and durable seawater electrolysis, ACS Appl. Mater. Interfaces. 17 (2025) 64340–64353.

[21] H. Liu, Z. Cui, Y. Sun, Z. Qiao, Y. Zhang, Q. Bai, Y. Wang, Synergistic design and synthesis of O, N Co-doped hierarchical porous carbon for enhanced supercapacitor performance, Energy Mater. 5 (2025) 500024.

[22] T. Kress, X. Liu, A.C. Forse, Pore network tortuosity controls fast charging in supercapacitors, Nat. Mater. 25 (2026) 440–446.

[23] M. Kuku, M. Arishi, Flexible and binder-free nickel-cobalt layered double hydroxides for high specific capacity supercapacitor applications, Mater. Chem. Phys. 332 (2025) 130230.

[24] X. Du, W. Han, X. Zhang, Application of in situ Raman and other technique in electrocatalytic water splitting, Int. J. Hydrog. Energy 200 (2026) 152928.

[25] T. Kansaard, T. Singha, S. Wannapop, A. Boonkitkoson, Y. Chuminjak, J. Sodtipinta, A. Somdee, Study of perovskite $NiMnO_3$, Mn_3O_4/$NiMnO_3$, and graphene oxide–Mn_3O_4/$NiMnO_3$ nanomaterials for use in symmetric and asymmetric supercapacitors, J. Alloys Compd. 1010 (2025) 178185.

[26] Z. Zhao, L. Sui, Z. Wang, S. Song, J. Wang, Y. Li, D. Zhao, G. Li, L. Miao, Enhanced electrocatalytic activity of NiCoP/Ni_5P_4@NiFe-LDH catalysts via Ir doping and oxygen vacancy engineering, Energy Mater. 6 (2026) 600025.

[27] L. Wang, L. Chen, R. Xu, M.A. Khan, J. Zhao, X. Yu, J. Björk, J. Rosen, J. Hu, Z. Chen, H. Zhao, Enhanced reaction kinetics of highly selective oxidation of 5-hydroxymethylfurfural to 2,5-furandicarboxylic acid over $NiCo_2S_4$, Nano Lett. 25 (2025) 14481–14488.

[28] Y. Wu, X. Du, X. Zhang, P doping transition metal sulfides as bifunctional electrocatalyst for overall seawater splitting, Int. J. Hydrog. Energy 103 (2025) 174–182.

[29] H. Ji, T. Wang, Y. Liu, C. Lu, G. Yang, W. Ding, W. Hou, A novel approach for sulfur-doped hierarchically porous carbon with excellent capacitance for electrochemical energy storage, Chem. Commun. 52 (2016) 12725–12728.

[30] L. Zhao, K. Meng, Y. Guo, Q. Wu, Q. Zhu, T. Zhou, Y. Fu, M. Wen, FeCoP sub-nanometric-sheets for electrocatalzing overall water splitting, Nano Res. Energy 3 (2024) e9120129.

[31] C. Liu, X. Chang, H. Mi, F. Guo, C. Ji, J. Qiu, Modulating pore nanostructure coupled with N/O doping towards competitive coal tar pitch-based carbon cathode for aqueous Zn-ion storage, Carbon 216 (2024) 118523.

[32] D. Dong, Y. Zhang, Y. Xiao, T. Wang, J. Wang, W. Gao, Mechanochemistry coupled with $MgCO_3$ one-step activation to prepare coal-based hierarchical porous carbon for supercapacitors, J. Power Sources 503 (2021) 230049.

[33] C. Hua, The honeysuckle stem derived porous carbon with an ultra-high specific surface area and ultra-long cycle life, J. Porous Mater. 30 (2023) 1763–1773.

[34] C. Yang, F. Song, Q. Chen, Composites of NiCo layered double hydroxide nanosheets and Co_3S_4 nanoparticles for asymmetric supercapacitors, ACS Appl. Nano Mater. 6 (2023) 10804–10816.

[35] Z. Li, H. Liu, Y.-H. Wang, S. Ji, Y. Zhang, Y. Liu, X. Lu, H. Teng, J.H. Horton, Y. Wang, X. Ma, Y.-J. Tang, Electronic structure modulation induced by the synergy of cobalt low-nuclearity clusters and mononuclear sites for efficient oxygen electrocatalysis, ACS Nano 19 (2024) 1600–1610.

[36] Y. Wu, X. Du, X. Zhang, Fe-doped $CoMoO_4$/Ni_3S_2 grown on Ni foam as a multifunctional electrode for electrocatalytic seawater and urea splitting, J. Alloys Compd. 1030 (2025) 180927.

[37] P.S. Dighe, R.S. Redekar, N.L. Tarwal, P.B. Sarawade, Design and development of the high-performance aqueous asymmetric supercapacitor based on the hydrothermally grown binder-less Ni-Co LDH nanosheets, J. Energy Storage 88 (2024) 111467.
[38] T. Yang, F. Yang, T. Wang, W. Zhang, F. Deng, C. Zhong, Q. Peng, C. Liu, X. Chen, Z. Zhang, Y. Li, Y. Feng, X. Li, K. Wang, C. Zhang, Y. Zhou, X. Lu, W. Zhu, Y. Wei, L. Xie, W. Huang, Gridized nanopolymer catalysis with atomically dispersed iron achieves the nearly 100% selective electrosynthesis of methanol from CO_2, Adv. Mater. 37 (2025) e2511233.
[39] T.O. John, O.'.M. Bockris, Mechanism of oxygen evolution on perovskites, J. Phys. Chem. 87 (1983) 2960–2971.